JPhys Energy

PAPER • OPEN ACCESS

A kinetic study on oxygen redox reaction of a double-perovskite reversible oxygen electrode—Part I: Experimental analysis

IOP Publishing J. Phys. Energy 6 (2024) 015011 https://doi.org/10.1088/2515-7655/ad0e29

Journal of Physics: Energy

CrossMark

OPEN ACCESS

RECEIVED
6 July 2023

REVISED
23 October 2023

ACCEPTED FOR PUBLICATION
20 November 2023

PUBLISHED
30 November 2023

PAPER

A kinetic study on oxygen redox reaction of a double-perovskite reversible oxygen electrode—Part I: Experimental analysis

Antonio Maria Asensio[1], **Fiammetta Rita Bianchi**[1,*], **Davide Clematis**[1], **Barbara Bosio**[1] **and Antonio Barbucci**[1,2]

[1] Department of Civil, Chemical and Environmental Engineering (DICCA), University of Genoa, Via Opera Pia 15, Genoa 16145, Italy
[2] Institute of Condensed Matter Chemistry and Technology for Energy, National Research Council (CNR-ICMATE), Via De Marini 6, 16149 Genova, Italy
[*] Author to whom any correspondence should be addressed.

E-mail: fiammettarita.bianchi@edu.unige.it

Keywords: solid oxide cells, double perovskite, oxygen reversible electrode, electrochemical impedance spectroscopy, DRT analysis

Abstract

The carbon-free energy transition requires the spread of advanced technologies based on high-performing materials. In this framework and particularly referring to electrochemical energy converting systems, double perovskites are arousing more and more interest as mixed ionic electronic conductors with flexible manufacturing, appropriate tailoring for many tasks and high chemical stability. Among their possible applications, they form excellent oxygen electrodes in solid oxide cell technology used as fuel cells, steam/CO_2 electrolysis cells and electrochemical air separation units. In view of the encouraging results shown by $SmBa_{1-x}Ca_xCo_2O_{5+\delta}$ co-doped double perovskite, this research work aims at a detailed analysis of $SmBa_{0.8}Ca_{0.2}Co_2O_{5+\delta}$ performance and the identification of kinetic paths for oxygen reduction and oxidation reactions. The electrochemical characterization was performed over a wide range of operation conditions to evaluate the electrode reversible behaviour and the interplay of the recognized phenomena governing the overall electrode kinetics.

1. Introduction

The success of the carbon-free energy transition is strictly related to the use of net-zero carbon energy sources that are substitutes for traditional fossil-based energy vectors. Nevertheless, completely phasing out fossil fuels is still far away and is a really hard task to reach worldwide. Many efforts throughout the scientific community and governments are being brought together to favour a fast and smooth energy transition [1].

Solid oxide cells (SOCs) are a high-performing and versatile solution which could make a pivotal contribution to this transition. Indeed, SOCs can work as power generators in fuel cell mode (SOFC—solid oxide fuel cell) and as energy storage systems in electrolysis (SOEC—solid oxide electrolysis cell). Additionally, their modularity allows their use at different scales. Several prototypes have been presented from portable applications, e.g. micro-SOFCs (μ-SOFCs) delivering power densities even higher than common Li-ion batteries [2] to residential and also large stationary co-generation plants up to MW power level [3, 4]. Unlike low temperature electrolysers, SOCs can produce pure hydrogen with a lower energy consumption as well as a syngas operating in co-electrolysis. Moreover, their use as a single unit with reversible operation makes such technology an ideal solution for the complex management of renewable energy sources [5–7]. A further possible SOC application, not fully exploited yet, is as electrochemical air separation unit to produce extremely pure oxygen from air by applying external power [8, 9].

Currently, the trend in SOC-based systems is moving towards intermediate temperature operating conditions to counteract the high costs and short lifetime related to cell component degradation. In this regard, secondary phase formation, element segregation, particle agglomeration and other microstructural changes are common phenomena induced by the high operating temperature [10, 11]. On the other hand, temperature reduction has a detrimental impact on both electrolyte ionic conductivity and electrode activity, penalizing the overall cell kinetics and performance. Therefore, the development of low-temperature, highly conductive electrolytes and efficient electrodes is a key aspect to foster SOC deployment.

Focusing on oxygen electrodes, several materials and crystallographic structures have been proposed [12–15] with extensive efforts towards nanostructural electrode engineering [16–18]. In recent years, studies on layered perovskites $AA'B_2O_{5+\delta}$ have led to the discovery of electroactive materials with impressive oxygen transport kinetics and significant stability. For instance, Lu *et al* coupled the high-performing A-site deficient double-perovskite $PrBa_{0.94}Co_2O_{5+\delta}$ with *in situ* nanoparticle exsolution, obtaining an electrode with very low polarization resistances and stable electrochemical performance [19]. Gumeci *et al* also reported on a praseodymium-based double perovskite consisting of $PrBa_{0.5}Sr_{0.5}Co_2O_{5+\delta}$ prepared by electrospinning and integrated in a conventional anode supported cell which reached a power density of 2.5 Wcm^{-2} at 750 °C under SOFC conditions [20]. Moreover, several studies have underlined the positive effects of calcium co-doping to increase material conductivity and lifetime in this kind of crystallographic structure. Yoo *et al* proved how Ca-doping into the A-site of $NdBaCo_2O_{5+\delta}$ double-perovskite enhances the redox stability and performance due to the affinity of the mobile oxygen species with calcium [13]. Choi *et al* proposed calcium doping for $PrBa_{0.5}Sr_{0.5-x}Ca_xCo_2O_{5+\delta}$, which induces an increase in oxygen vacancy concentration [21]. Analysing $PrBaCo_2O_{5+\delta}$ double perovskite co-doped with calcium, Xia *et al* observed a reduction of the thermal expansion coefficient that constitutes a further key point to stabilize the electrode [22]. In line with the introduction of different co-doping elements, Lee *et al* quantitatively assessed the cation segregation induced by cation size mismatch. The authors computationally predicted the suppression of the segregated oxides by the incorporation of calcium which was further experimentally validated [23].

In this framework, the authors propose an innovative reversible oxygen electrode starting from well-known Ba and Co-based structures but with a higher performance and a still possible microstructural improvement by optimising the synthesis procedure. It consists of $SmBa_{0.8}Ca_{0.2}Co_2O_{5+\delta}$ (SBCCO) double perovskite with an optimised Ca co-doped concentration in the A-site according to the authors' previous study, where a preliminary analysis was performed through a limited set of working conditions aimed at the evaluation of material feasibility [24]. In view of the promising operation shown by the 20% Ca-doped sample compared to other compositions, a more detailed electrochemical characterization with a physically based explanation of the mechanisms involved was necessary before further optimization towards commercial manufacturing and use requirements. Here, a wider range of operating conditions, varying temperatures and gas compositions, were analysed through electrochemical impedance spectroscopy (EIS) measurements on symmetrical cells. Comprehension of the oxygen redox reaction features was achieved through distributions of relaxation times (DRT) analysis, which aided in the identification of the main processes governing oxygen reduction and evolution reactions (ORR/OER) by pointing out the rate-determining steps and their interplay depending on the working conditions. This laid the foundations for a specific model formulation presented in the second part of the study.

2. Experimental

2.1. Cell preparation

Referring to electrode manufacturing, SBCCO powder was synthesized by following a modified Pechini's route starting from nitrate metal precursors with the required molar ratios and adding the complexing agents ethylenediaminetetraacetic acid and citric acid. The resulting mixture was dissolved in deionized water. The solution was then heated till a red, viscous gel was formed. This gel was calcined at 900 °C for 10 h in air to obtain the crystallized powder. A detailed description of the synthesis method has already been reported elsewhere [24, 25].

In order to produce a dense thick electrolyte pellet, $Sm_{0.2}Ce_{0.8}O_{2-\delta}$ (SDC—samarium doped ceria) powders from FuelCellMaterials (SDC20-HP) were cold-pressed at 40 MPa and sintered at 1450 °C for 5 h leading to a 20 mm button cell electrolyte pellet. On top of the sintered pellet, a rough SDC layer was deposited by wet powder spraying of an ethanol dispersion of SDC powder and polyvinylpyrrolidone as dispersant (1 wt.%) and then sintered at 1250 °C for 2 h. The role of the sprayed SDC layer is to enhance the adhesion of the electrode to the electrolyte.

SBCCO powders were magnetically dispersed in α-terpineol till a homogeneous ink was obtained. Then, the electrode ink was slurry-coated on both sides of the SDC electrolyte pellet and sintered at 1050 °C for 2 h. Finally, a set of electrolyte supported cells with a geometrical active electrode area of 0.28 cm^2 was obtained.

2.2. Crystallographic and morphological characterization

The crystallographic characterization of the synthesized powders was performed by x-ray diffraction (XRD) carrying out the analysis by the PANalytical AERIS diffractometer (Co Kα radiation, range 20–80°, step size 0.02° and PIXCEL1D detector). The Rietveld refinement was carried out to determine the crystallographic phase of the electrocatalyst using the FullProf Suite software [26]. The morphological characterization of the prepared electrodes was performed through scanning-electrode microscopy (Phenom-ProX).

2.3. Electrochemical characterization

The prepared electrolyte supported symmetrical cells were placed inside an in-house-built test-rig for the electrochemical characterization. Two platinum nets were used on both the working electrode and the counter electrode surfaces acting as current collectors. The system was heated at a rate of 1.0 °C min^{-1} up to the testing temperature. The measurements were performed in a two-electrode configuration at open circuit voltage (OCV) by using a potentiostat coupled to a frequency response analyser (Metrohm Autolab PGSTAT302 N). Impedance measurements were carried out in a frequency range of 1 MHz–0.01 Hz, with 12 points per frequency decade, in potentiostatic mode between 500 °C and 750 °C as the temperature range. Different N_2/O_2 mixtures were fed during the whole experimental campaign maintaining a gas flow rate of 30 NmL min^{-1} on each side of the cell. The oxygen partial pressures were varied from 1 to 0.05 atm. Before starting any systematic analysis, the linearity of the current response to the input voltage perturbation was checked. This was verified by applying different voltage perturbation amplitudes ranging from 5 to 25 mV [27]. The EIS results were then analysed by a DRT tool developed by the authors [28]. The algorithm, called extended domain- DRT (ED-DRT), is based on a zero-padding technique which is an approach widely used in signal theory. As discussed in [28], this methodology reduces the issues about domain truncation and discretization required for the application of the Tikhonov regularization method. It has also been demonstrated that the ED-DRT algorithm is less sensitive to experimental noise with fewer artefacts appearing in the DRT curve. The regularization parameter λ was evaluated by the *L*-curve method [29, 30].

3. Results and discussion

3.1. Microstructural and crystallographic analysis

The cross-section of the symmetrical cell and its top view, presented in figures 1(a) and (b), were analysed to evaluate sample microstructure and features. Indeed, electrode thickness, porosity and electrocatalyst grain size are well known to play a relevant role in cell performance in terms of charge transfer kinetics and gas mass transport [31, 32]. The microscope observations highlight a good electrode/electrolyte interface characterized by an electrode well adhered to the electrolyte. The applied air-sprayed SDC successfully contributes to this result. In addition, the electrode shows a constant thickness along the overall cell equal to 35 μm as well as a suitable porosity (figure 1(a)). Furthermore, the SBCCO grain size distribution is quite homogeneous with diameters ranging from 0.5 to 2 μm (figure 1(b)).

The XRD pattern for the as-synthesized SBCCO powder is shown in figure 1(c). XRD reveals twin peaks typical of the tetragonal space group *P4/mmm* for the layered perovskite structure as the main phase. A minor secondary phase corresponding to the *Pm-3m* is also detected. Consequently, Rietveld refinement was performed to quantify the purity of the synthesized powder and the calculated profile results in good agreement with the XRD data (figure 1(d)). The peaks related to the secondary phase (♦) well match with those of a simple perovskite structure, reasonably grown due to the segregation induced by the size difference between the large ionic radius of Ba (1.49 Å) and the small radius of the doping Ca (1.14 Å). This phenomenon has already been seen in previous works on double perovskite synthesis and has usually been attributed to the large difference in ionic radii of the doping elements [24, 33]. Thus, the partial substitution of a larger size Ba^{2+} ion by a smaller size Ca^{2+} ion leads to the formation of the single perovskite *Pm-3m* $SmCoO_{3-\delta}$ when the total amount of doping is not incorporated inside the *P4/mmm* crystallographic lattice. In addition, even if the segregated phase is characterized by a lower conductivity, the doping effect on the main crystallographic structure usually predominates (as highlighted following by the EIS measurements) but also due to the small present amount of this less conductive phase [34]. This was also verified for analysed samples, as shown in table 1 which reports the structure lattice parameters of two phases and their relative amounts calculated by Rietveld analysis. Indeed, the segregated phase is below 3%.

3.2. Electrochemical characterization

In order to identify the electrochemical activity of the SBCCO electrode, EIS was conducted on symmetric cells within the temperature range of 500 °C–750 °C in ambient air under OCV conditions followed by DRT analysis to characterize different occurring phenomena in detail. The measurements show fast kinetics of the oxygen redox reaction with an overall polarization resistance ranging from 3.3 to 0.04 Ωcm^2 at 500 °C and 750 °C, respectively (figure 2(a)), obtaining results quite similar to those of previously tested samples by the authors under identical working conditions [24].

The obtained polarization resistance (R_p) values are reported in table 2 and compared to the performance of some well-known and still under research materials applied as SOC oxygen electrodes.

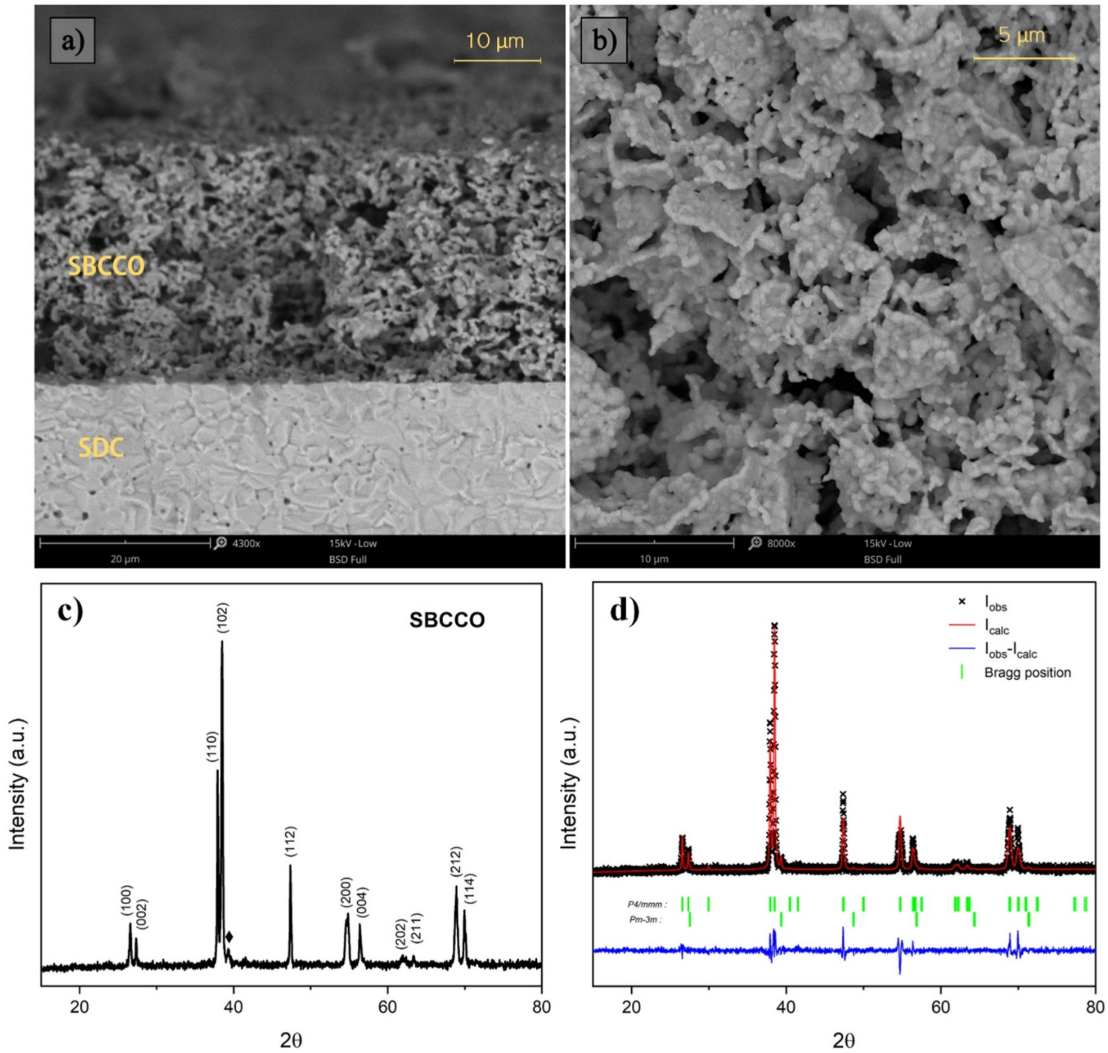

Figure 1. Microstructural and crystallographic analysis on SBCCO electrode and powder: SEM micrographs of the (a) cross-section and (b) top view of the electrode; (c) XRD pattern and (d) Rietveld analysis with distinctive peaks attributed to the secondary phase marked by ♦.

Table 1. Unit cell parameters obtained by Rietveld analysis for SBCCO material.

	$SmBa_{0.8}Ca_{0.2}Co_2O_{5+\delta}$	
	P4/mmm	*Pm-3m*
Relative amount (%)	97.19 (±0.94)	2.81 (±0.21)
V (Å^3)	114.963 (8)	53.216 (11)
A=B (Å)	3.89475	3.76138
C (Å)	7.57904	3.76138

SBCCO shows lower values with respect to the classic materials and comparable results with the best-performing ones [35, 36]. Nevertheless, considering the simple electrode architecture proposed in this work (i.e. slurry coated), SBCCO performance is likely to be improved by electrode architecture engineering with the incorporation of a composite electrode [37], exsolved nanoparticles [38, 39] or electrocatalyst infiltration [40].

The EIS data reveal different phenomena involved in the electrochemical reactions which deserves an accurate analysis. Specifically, above 650 °C a process, which cannot be visually recognised at lower temperatures, starts to be relevant as shown in figure 2(a) inset. The DRT analysis was performed to investigate the process characteristic peak frequencies. From the DRT results shown in figure 2(b), two main peaks are distinguished in lower temperature tests (500 °C–600 °C), while at higher temperatures (650 °C–750 °C) three peaks are visible which are correlated to the observed slight change of EIS shape in the low-frequency domain. The new, third peak at temperatures higher than 600 °C appears between 0.1 and

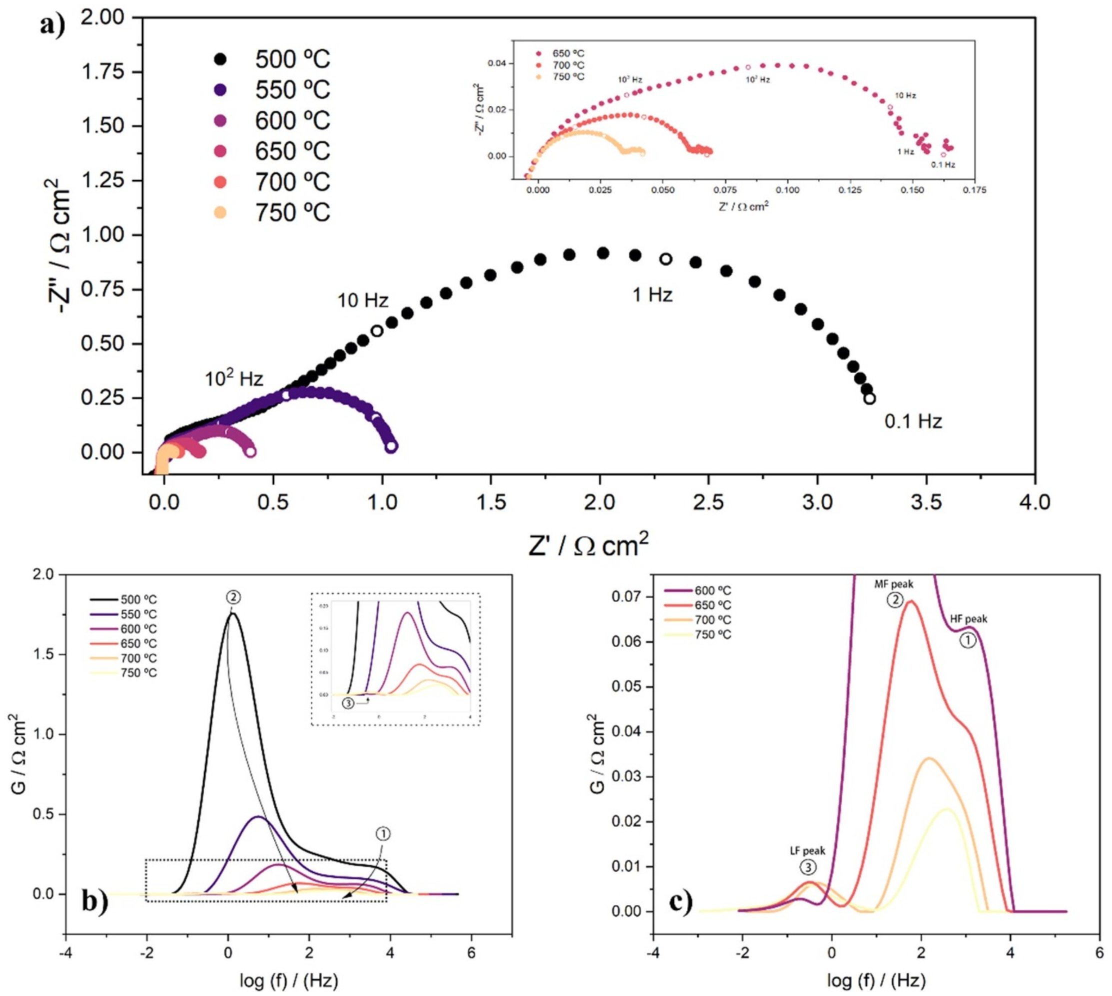

Figure 2. (a) Nyquist plots of symmetrical SBCCO half-cell measured at OCV over a 500 °C–750 °C temperature range under ρO_2: 0.21 atm, highlighting the 650 °C−750 °C temperature range in the inset (the electrolyte resistance has been removed), (b) derived DRT analysis profiles and (c) the profiles over 600 °C–750 °C.

1 Hz (figure 2(c)). From the DRT analysis, this peak is already visible at 600 °C but it acquires a well-defined shape only at higher temperatures. These three peaks/processes involved in the overall redox reaction are in the following paragraphs and figures identified as: HF at high frequency, MF at middle frequency and LF at low frequency. From figures 2(b) and (c) it is also noteworthy that while the characteristic time constant of LF peak is nearly independent of temperature, HF and MF peaks tend to merge at higher temperatures. The characteristic frequency of the MF peak moves quickly towards the HF peak one, indicating a highly thermally activated process; consequently, a single peak is visible at 750 °C. Nevertheless, both HF and MF peaks could be deconvoluted thanks to their observed trends over the whole investigated temperature range.

In order to have a first insight of the temperature dependences, the overall polarization resistance R_p and the single resistances R_HF, R_MF and R_LF, referred to the high, middle and low frequency terms, respectively, were evaluated by defining a limited frequency range for each peak and calculating the area under the curve. Indeed, the size of the peaks in DRT diagrams represents a resistance. The obtained values are reported in figure 3 according to an Arrhenius formulation (equation (1)):

$$R = A\exp^{-\left(\frac{E_\mathrm{a}}{k_\mathrm{B}T}\right)}, \tag{1}$$

where A is the pre-exponential coefficient, E_a the activation energy, k_B the Boltzmann constant and T the temperature.

The data show a good linearity enabling the determination of the activation energies E_a for the total polarization resistance as well as for the high- and medium-frequency resistances within the whole temperature range. In contrast, the low-frequency peak shows a weak thermal dependence, resulting in a slightly increasing trend as the temperature is raised. A global E_a equal to 1.19 eV and specific E_a values of 0.92 eV for the HF and 1.45 eV for the MF processes were obtained. This is in line with figure 2(b) where the

Table 2. Polarization resistance comparison between well-known and under research materials recorded at OCV and pO_2: 0.21 atm.

Material	Value	References
	Well-known electrodes	
LSM-YSZ ($La_{0.8}Sr_{0.2}MnO_3$—Y_2O_3/ZrO_2)	2.35 Ωcm^2 @650 °C 0.69 Ωcm^2 @700 °C	[41]
LSCF ($La_{0.6}Sr_{0.4}Co_{0.2}Fe_{0.8}O_{3+\delta}$)	2.39 Ωcm^2 @600 °C 0.81 Ωcm^2 @650 °C 0.35 Ωcm^2 @700 °C	[42]
LSC-SDC ($La_{0.6}Sr_{0.4}CoO_{3-\delta}$—$Sm_{0.2}Ce_{0.8}O_{2-\delta}$)	0.32 Ωcm^2 @700 °C	[43]
BSCF ($Ba_{0.5}Sr_{0.5}Co_{0.8}Fe_{0.2}O_{3-\delta}$)	0.06–0.07 Ωcm^2 @600 °C 0.46 Ωcm^2 @600 °C	[44] [45]
	Under research electrodes	
LNO ($La_2NiO_{4+\delta}$)	0.85 Ωcm^2 @600 °C	[46]
SFSO ($SrFe_{0.85}Si_{0.15}O_{3-\delta}$)	0.24 Ωcm^2 @600 °C	[47]
BSFP ($Bi_{0.5}Sr_{0.5}Fe_{0.95}P_{0.05}O_{3-\delta}$)	0.18 Ωcm^2 @700 °C	[47]
PBCCO ($PrBa_{0.8}Ca_{0.2}Co_2O_{5+\delta}$)	0.02 Ωcm^2 @750 °C	[48]
SBCO-SDC ($SmBaCo_2O_{5+\delta}$—$Sm_{0.2}Ce_{0.8}O_{2-\delta}$)	0.16 Ωcm^2 @700 °C	[49]
PCBCCO ($Pr_{0.9}Ca_{0.1}Ba_{0.8}Ca_{0.2}Co_2O_{5+\delta}$)	0.28 Ωcm^2 @600 °C	[22]
SBCCO ($SmBa_{0.8}Ca_{0.2}Co_2O_{5+\delta}$)	0.394 Ωcm^2 @600 °C 0.162 Ωcm^2 @650 °C 0.068 Ωcm^2 @700 °C 0.041 Ωcm^2 @750 °C	This work

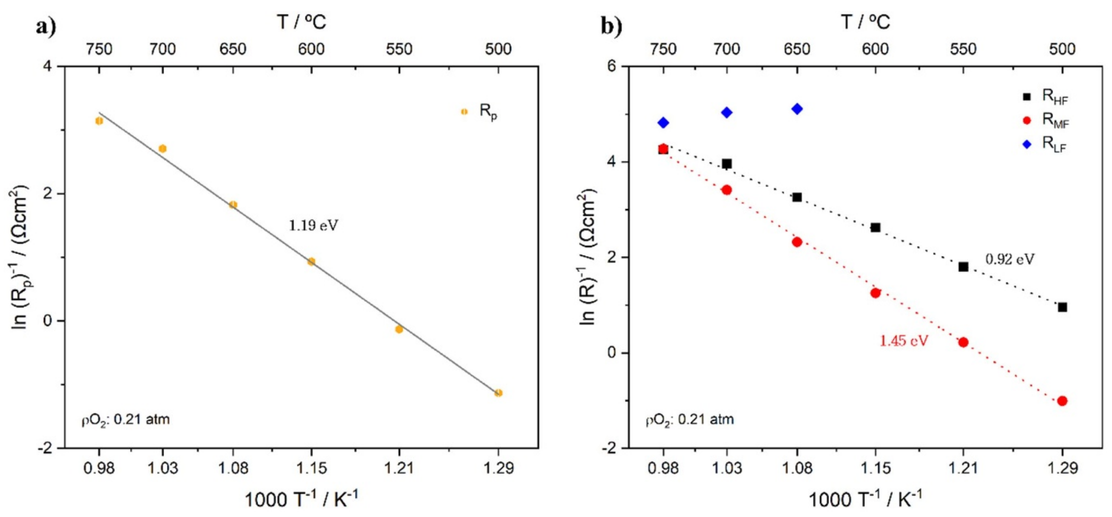

Figure 3. Arrhenius plots of (a) the overall half-cell polarization resistance R_p and (b) R_{HF}, R_{MF} and R_{LF} as a function of the temperature at ρO_2: 0.21 atm according to DRT analysis.

MF process is shown to be much more affected by the temperature change. SBCCO has a lower value of global E_a with respect to commonly used LSM-YSZ (lanthanum strontium manganite/yttria stabilized zirconia) and LSCF (lanthanum strontium cobalt ferrite) electrodes, where the reported values range between 1.2 and 1.6 eV [50–53]. Moreover, in mixed ionic and electronic conductor (MIEC) electrocatalysts two thermally dependent processes are frequently identified. For instance, a $Ba_{0.5}Sr_{0.5}Co_{0.8}Fe_{0.2}O_3$ electrode showed an E_a of 0.85 eV and 1.31 eV for high- and low-frequency arcs, respectively [45]. Similarly, in an optimised composite configuration consisting of LSM mixed with different ionic conductor oxides, two characteristic processes were identified with activation energies equal to ~1 eV and ~1.4 eV [54].

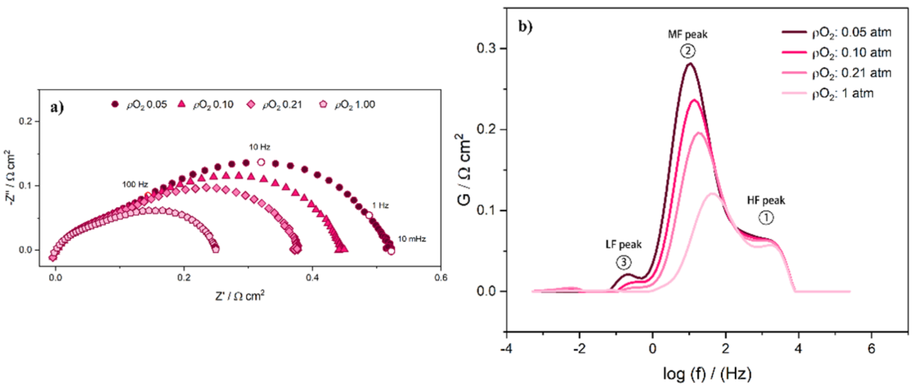

Figure 4. EIS plots measured at OCV at 600 °C at different oxygen partial pressures (a) and corresponding DRT analysis profiles (b) referring to half-cell resistance values.

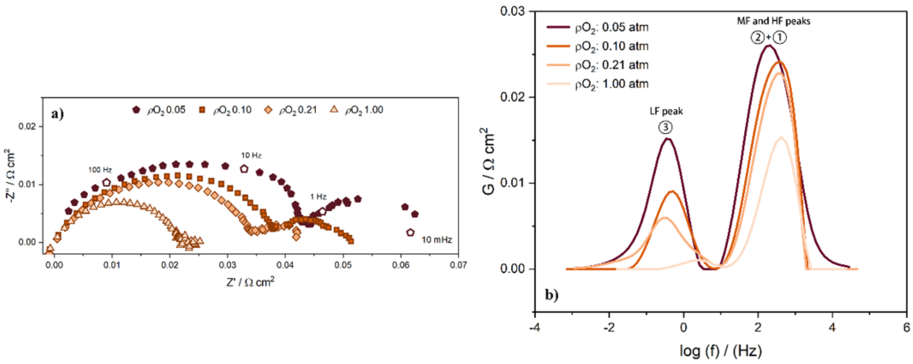

Figure 5. EIS plots measured at OCV at 750 °C at different oxygen partial pressures (a) and corresponding DRT analysis profiles (b) referring to half-cell resistance values.

Although in some of the literature the identification of reaction mechanisms has just been based on E_a values and specific relaxation times, it should be considered that each electrode material involves many peculiar variables, e.g. microstructure, composition, interfaces, and current collectors, resulting in some discrepancies among reference studies [15, 47, 54, 55]. Here, to have a clear evaluation of the specific reaction path characterizing the SBCCO system and to determine the bottleneck of the overall process, the oxygen partial pressure dependence on electrode activity was also investigated.

Figures 4 and 5 show the dependence of the EIS spectra on oxygen partial pressure and their corresponding DRT-derived profiles at 600 °C and 750 °C, respectively. As can be seen in figure 4(b) at 600 °C, the LF peak does not become visible until a partial pressure lower than 0.1 atm underlining the large influence of the oxygen partial pressure. In contrast, the HF peak does not show any remarkable dependence on fed gas. In fact, from the Nyquist plot (figure 4(a)), the high-frequency data obtained points stack on top of each other despite the gas composition, while the MF peak is again highly affected by the oxygen partial pressure variation. Referring to the 750 °C case, figure 5 shows that both visible peaks are influenced by the fed gases.

The influence of the partial pressure over the total R_p for both temperatures is represented in figure 6, assuming a general formulation for the relationship between the resistance R and the oxygen partial pressure pO_2 (equation (2)):

$$R = B\,(p_{O_2})^{-m}, \tag{2}$$

where B is the constant pre-exponential coefficient and m the oxygen order. The evaluated m-value ranges from 0.245 to 0.307 from 600 °C to 750 °C. The variation of its value as the temperature increases is clear evidence of change of the process controlling steps. Indeed, the LF peak is almost negligible at 600 °C, except at $pO_2 = 0.05$ atm, whereas it is clearly visible at 750 °C for all measurements. In order to verify the influence of the process at low frequency ③ on the oxygen order value, a third set of data points without this contribution was plotted for 750 °C. As can be observed, in this case the obtained m-value of 0.256 is close to that at 600 °C suggesting an equal reaction path for HF and MF processes independent of temperature.

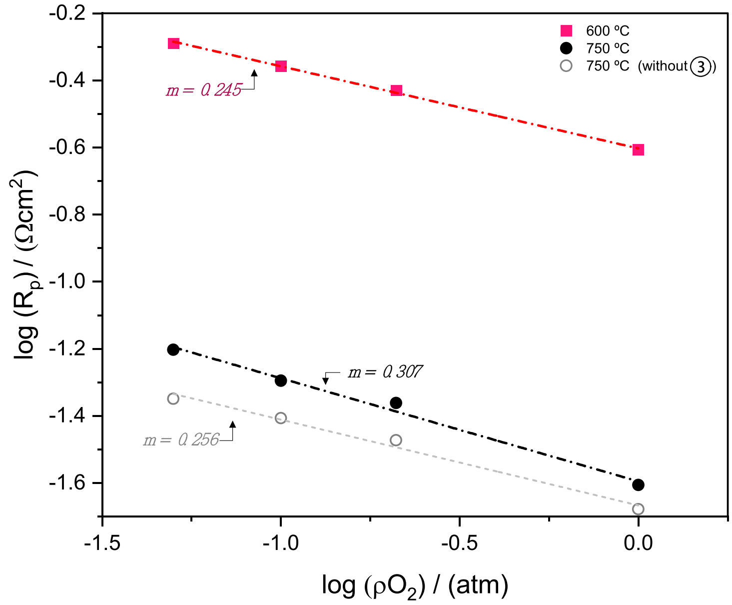

Figure 6. Influence of the oxygen partial pressure on overall half-cell polarization resistance R_p at 600 °C and 750 °C according to DRT analysis (③ refers to low frequency process).

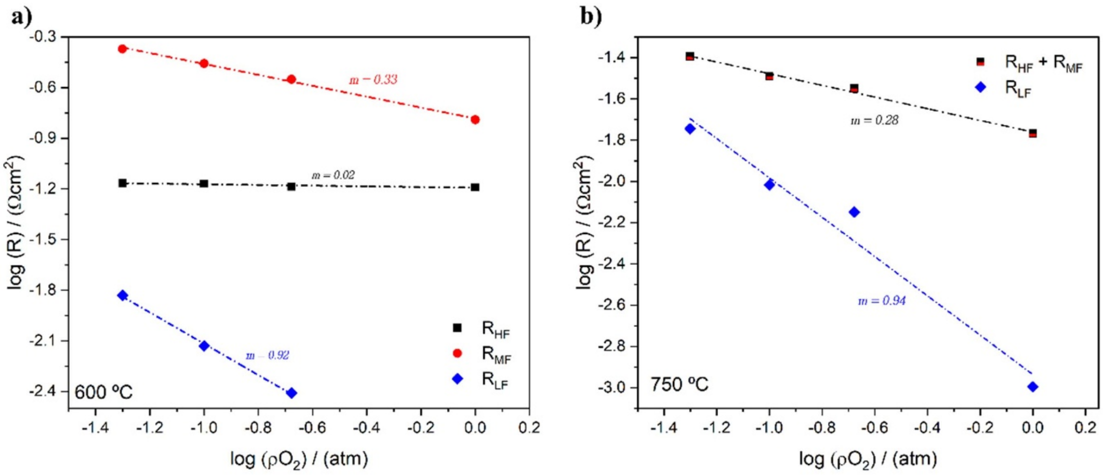

Figure 7. Dependence of the single process half-cell resistances on the oxygen partial pressure at 600 °C (a) and at 750 °C (b) from DRT analysis.

Figure 7 reports the oxygen partial pressure dependency of the characteristic resistances for each frequency range at two tested temperatures. Both at 600 °C and 750 °C LF values have a high dependence resulting in *m*-values of 0.92 and 0.94, respectively, unlike the other peaks where the influence is lower for MF (0.28 and 0.33) and negligible for HF.

3.3. Kinetic path identification

According to previous references on MIEC oxygen electrodes [46, 55, 56], the oxygen redox reaction mechanism consists of a series of steps, here listed:

a. Molecular oxygen diffusion into porous MIEC;
b. Molecular oxygen adsorption on MIEC surface (equation (3))

$$O_{2(g)} \rightleftharpoons O_{2(\mathrm{ad})}; \tag{3}$$

c. Adsorbed molecular oxygen surface dissociation (equation (4))

$$O_{2(\mathrm{ad})} \rightleftharpoons 2O_{(\mathrm{ad})}; \tag{4}$$

d. Atomic adsorbed oxygen surface exchange with MIEC bulk material (equation (5))

$$2O_{(\mathrm{ad})} + 2V_{o}^{\cdot\cdot}\ (\mathrm{MIEC}) + 4e' \rightleftharpoons 2O_{o}^{x}\ (\mathrm{MIEC}); \tag{5}$$

e. Oxygen bulk diffusion within MIEC material through vacancy hopping;
f. Oxygen transfer at MIEC electrode–electrolyte interface (equation (6))

$$2O_{o}^{x}\ (\mathrm{MIEC}) + 2V_{o}^{\cdot\cdot}\ (\mathrm{Electrolyte}) \rightleftharpoons 2O_{o}^{x}\ (\mathrm{Electrolyte}) + 2V_{o}^{\cdot\cdot}\ (\mathrm{MIEC}). \tag{6}$$

All these steps are correlated to the oxygen partial pressure in different ways. Indeed, mechanisms such as gas diffusion and adsorption/desorption have the highest dependence resulting in an m-value equal to 1, whereas the dissociation adsorption and the atomic oxygen diffusion usually show a lower influence of around 0.5. Phenomena of oxygen transfer at the gas–solid interface and the electrode–electrolyte interface have a dependence of 0.25 [45].

Referring to this reaction path and considering the electrochemical characterization performed, the following conclusions can be formulated about SBCCO characteristic processes:

- the HF contribution, showing independence from gas composition and favoured on temperature increase ($E_a = 0.92$ eV), can be due to processes at the electrode–electrolyte interface where the oxygen ions have to be transferred [57];
- the MF contribution is correlated with a thermally activated mechanism ($E_a = 1.45$ eV) dependent on gas composition. Moreover, the detected m-values ranging between 0.28 and 0.33 suggest an intermediate step between the adsorption process and the oxygen exchange reaction, prevailing as a function of temperature. Here, the MF contribution can involve oxygen surface mechanisms [45, 55];
- the LF contribution has a low thermal dependency, while it shows a high dependence on gas composition ($m \approx 1$) meaning molecular oxygen is involved as in gas transport [45, 57].

These results provide (a) the indications to drive the realization of a tailored electrode architecture likely to further enhance the oxygen redox reactions, and (b) the basis for the development of a mechanistic model able to predict SBCCO electrode behaviour under variable working conditions. Indeed, starting from experimental observations, a clear interpretation of observed phenomena derives from the identification of the limiting steps for oxygen redox reactions and the verification of the assumed kinetics path through a detailed physics-based modelling of electrode performance.

4. Conclusions

Despite the extensive number of research papers focused on the development of high-performing SOC electrocatalysts characterized by low polarization resistances and high thermal and chemical stabilities, studies of new solutions able to cope with the demanding task of operating in reversible SOC are still necessary. The key to optimize active electrodes lies in the material itself and in electrode architectures tailoring the material properties. Understanding the phenomena behind the overall measured performance has also become a fundamental aspect in driving the optimization of the components. Double perovskites are a very interesting class of materials as reversible oxygen electrodes for SOC technology; nevertheless, all their properties and potentialities are still partially unexplored. In this context, the authors report the results on SBCCO, a double perovskite successfully modified to increase the oxygen surface exchange activity and ionic transport, achieving an overall resistance of 0.04 Ω cm^2 at 750 °C with a basic electrode configuration. Moreover, the experimental data analysis through DRT allowed the study of the mechanisms that control the ORR/OER.

In summary, three processes were identified with relaxation times at high, medium and low frequencies (noted as HF, MF and LF). MF and HF processes have a strong dependence on the thermal regime with 1.45 eV and 0.92 eV as the activation energy values, respectively. LF is only visible at high temperatures when HF and MF are fully activated or at very low oxygen partial pressures. Measurements devoted to the evaluation of the oxygen partial pressure dependencies showed how the LF process is significantly more sensitive to gas composition compared to the others, above all with respect to the HF process which has no significant variation. A literature survey on similar materials and evidence from the results obtained here allowed a SBCCO-specific kinetic path to be proposed. Three processes detected at LF, MF and HF are associated with gas transport, oxygen exchange at the SBCCO surface and ion transfer at the electrolyte interface, respectively. As a result, based on the applied working conditions, one of the discerned processes will become the rate-determining step.

This analysis has formed the basis for a robust modelling activity which will be presented in a forthcoming communication.

Data availability statement

The data that support the findings of this study are available upon reasonable request to the authors.

Funding

This research was developed within the project 'Network 4 Energy Sustainable Transition—NEST' funded under the National Recovery and Resilience Plan (NRRP), Mission 4 Component 2 Investment 1.3—Call for Tender No. 1561 of 11.10.2022 of Ministero dell'Università e della Ricerca (MUR); funded by the European Union—NextGenerationEU.

ORCID iDs

Antonio Maria Asensio https://orcid.org/0000-0003-4390-0212
Fiammetta Rita Bianchi https://orcid.org/0000-0001-5218-2828

References

[1] Vanegas Cantarero M M 2020 Of renewable energy, energy democracy, and sustainable development: a roadmap to accelerate the energy transition in developing countries *Energy Res. Social Sci.* **70** 101716
[2] Evans A, Bieberle-Hütter A, Rupp J L M and Gauckler L J 2009 Review on microfabricated micro-solid oxide fuel cell membranes *J. Power Sources* **194** 119–29
[3] Becker W L, Braun R J, Penev M and Melaina M 2012 Design and technoeconomic performance analysis of a 1MW solid oxide fuel cell polygeneration system for combined production of heat hydrogen, and power *J. Power Sources* **200** 34–44
[4] Bertoldi M, Bucheli O F and Ravagni A 2017 Development, manufacturing and deployment of SOFC-based products at SOLIDpower *ECS Trans.* **78** 117
[5] Ebbesen S D, Knibbe R and Mogensen M 2012 Co-electrolysis of steam and carbon dioxide in solid oxide cells *J. Electrochem. Soc.* **159** F482
[6] Hauch A, Küngas R, Blennow P, Hansen A B, Hansen J B, Mathiesen B V and Mogensen M B 2020 Recent advances in solid oxide cell technology for electrolysis *Science* **370** eaba6118
[7] Bianchi F R and Bosio B 2021 Operating principles, performance and technology readiness level of reversible solid oxide cells *Sustainability* **13** 4777
[8] Sadykov V A *et al* 2020 Novel materials for solid oxide fuel cells cathodes and oxygen separation membranes: fundamentals of oxygen transport and performance *Carbon Resour. Convers.* **3** 112–21
[9] Sunarso J, Hashim S S, Zhu N and Zhou W 2017 Perovskite oxides applications in high temperature oxygen separation, solid oxide fuel cell and membrane reactor: a review *Prog. Energy Combust. Sci.* **61** 57–77
[10] McPhail S J *et al* 2022 Addressing planar solid oxide cell degradation mechanisms: a critical review of selected components *Electrochem. Sci. Adv.* **2** e2100024
[11] Zarabi Golkhatmi S, Asghar M I and Lund P D 2022 A review on solid oxide fuel cell durability: latest progress mechanisms, and study tools *Renew. Sustain. Energy Rev.* **161** 112339
[12] Sun C, Hui R and Roller J 2010 Cathode materials for solid oxide fuel cells: a review *J. Solid State Electrochem.* **14** 1125–44
[13] Yoo S, Jun A, Ju Y-W, Odkhuu D, Hyodo J, Jeong H Y, Park N, Shin J, Ishihara T and Kim G 2014 Development of double-perovskite compounds as cathode materials for low-temperature solid oxide fuel cells *Angew. Chem., Int. Ed.* **53** 13064–7
[14] Amow G, Davidson I J and Skinner S J 2006 A comparative study of the Ruddlesden-Popper series, $La_{n+1}Ni_nO_{3n+1}$ (n=1, 2 and 3), for solid-oxide fuel-cell cathode applications *Solid State Ion.* **177** 1205–10
[15] Richter J, Holtappels P, Graule T, Nakamura T and Gauckler L J 2009 Materials design for perovskite SOFC cathodes *Monatshefte für Chemie* **140** 985–99
[16] Ding D, Li X, Lai S Y, Gerdes K and Liu M 2014 Enhancing SOFC cathode performance by surface modification through infiltration *Energy Environ. Sci.* **7** 552–75
[17] Tsekouras G, Neagu D and Irvine J T S 2013 Step-change in high temperature steam electrolysis performance of perovskite oxide cathodes with exsolution of B-site dopants *Energy Environ. Sci.* **6** 256–66
[18] Asensio A M, Clematis D, Viviani M, Carpanese M P, Presto S, Cademartori D, Cabot P L and Barbucci A 2021 Impregnation of microporous SDC scaffold as stable solid oxide cell BSCF-based air electrode *Energy* **237** 121514
[19] Lu F, Xia T, Li Q, Wang J, Huo L and Zhao H 2019 Heterostructured simple perovskite nanorod-decorated double perovskite cathode for solid oxide fuel cells: highly catalytic activity, stability and CO_2-durability for oxygen reduction reaction *Appl. Catal.* B **249** 19–31
[20] Gumeci C, Parrondo J, Hussain A M, Thompson D and Dale N 2021 Praseodymium based double-perovskite cathode nanofibers for intermediate temperature solid oxide fuel cells (IT-SOFC) *Int. J. Hydrog. Energy* **46** 31798–806
[21] Choi S, Park S, Shin J and Kim G 2015 The effect of calcium doping on the improvement of performance and durability in a layered perovskite cathode for intermediate-temperature solid oxide fuel cells *J. Mater. Chem.* A **3** 6088–95

[22] Xia W, Liu X, Jin F, Jia X, Shen Y and Li J 2020 Evaluation of calcium codoping in double perovskite $PrBaCo_2O_{5+\delta}$ as cathode material for IT-SOFCs *Electrochim. Acta* **364** 137274
[23] Lee W, Han J W, Chen Y, Cai Z and Yildiz B 2013 Cation size mismatch and charge interactions drive dopant segregation at the surfaces of manganite perovskites *J. Am. Chem. Soc.* **135** 7909–25
[24] Asensio A M, Clematis D, Cademartori D, Carpanese M P, Viviani M, Carbone C and Barbucci A 2023 Calcium doping in double perovskite $SmBa_{1-x}Ca_xCo_2O_{5+\delta}$ to enhance the electrochemical activity of solid oxide cell reversible oxygen electrode *J. Alloys Compd.* **933** 167731
[25] Martynczuk J, Arnold M, Wang H, Caro J and Feldhoff A 2007 How $(Ba_{0.5}Sr_{0.5})(Fe_{0.8}Zn_{0.2})O_{3-\delta}$ and $(Ba_{0.5}Sr_{0.5})(Co_{0.8}Fe_{0.2})O_{3-\delta}$ perovskites form via an EDTA/citric acid complexing method *Adv. Mater.* **19** 2134–40
[26] Rodríguez-Carvajal J 1993 Recent advances in magnetic structure determination by neutron powder diffraction *Physica* B **192** 55–69
[27] Macdonald J R and Johnson W B 2005 Fundamentals of Impedance Spectroscopy *Impedance Spectroscopy* (Wiley) pp 1–26
[28] Clematis D, Ferrari T, Bertei A, Asensio A M, Carpanese M P, Nicolella C and Barbucci A 2021 On the stabilization and extension of the distribution of relaxation times analysis *Electrochim. Acta* **391** 138916
[29] Calvetti D, Morigi S, Reichel L and Sgallari F 2000 Tikhonov regularization and the L-curve for large discrete ill-posed problems *J. Comput. Appl. Math.* **123** 423–46
[30] Boukamp B A 2020 Distribution (function) of relaxation times, successor to complex nonlinear least squares analysis of electrochemical impedance spectroscopy? *J. Phys. Energy* **2** 042001
[31] Smith J R, Chen A, Gostovic D, Hickey D, Kundinger D, Duncan K L, DeHoff R T, Jones K S and Wachsman E D 2009 Evaluation of the relationship between cathode microstructure and electrochemical behavior for SOFCs *Solid State Ion.* **180** 90–98
[32] Bertei A, Barbucci A, Carpanese M P, Viviani M and Nicolella C 2012 Morphological and electrochemical modeling of SOFC composite cathodes with distributed porosity *Chem. Eng. J.* **207–208** 167–74
[33] Kim J H, Prado F and Manthiram A 2008 Characterization of $GdBa_{1-x}Sr_xCo_2O_{5+\delta}$ $(0 \leqslant x \leqslant 1.0)$ double perovskites as cathodes for solid oxide fuel cells *J. Electrochem. Soc.* **155** B1023
[34] Lim C, Jun A, Jo H, Ok K M, Shin J, Ju Y-W and Kim G 2016 Influence of Ca-doping in layered perovskite $PrBaCo_2O_{5+\delta}$ on the phase transition and cathodic performance of a solid oxide fuel cell *J. Mater. Chem.* A **4** 6479–86
[35] Pelosato R, Cordaro G, Stucchi D, Cristiani C and Dotelli G 2015 Cobalt based layered perovskites as cathode material for intermediate temperature solid oxide fuel cells: a brief review *J. Power Sources* **298** 46–67
[36] Irvine J *et al* 2021 Roadmap on inorganic perovskites for energy applications *J. Phys. Energy* **3** 031502
[37] Tarutin A P, Filonova E A, Ricote S, Medvedev D A and Shao Z 2023 Chemical design of oxygen electrodes for solid oxide electrochemical cells: a guide *Sustain. Energy Technol. Assess.* **57** 103185
[38] Mei J, Liao T and Sun Z 2023 Metal exsolution engineering on perovskites for electrocatalysis: a perspective *Mater. Today Energy* **31** 101216
[39] Neagu D *et al* 2023 Roadmap on exsolution for energy applications *J. Phys. Energy* **5** 031501
[40] Niu Y, Huo W, Yu Y, Li W, Chen Y and Lv W 2022 Cathode infiltration with enhanced catalytic activity and durability for intermediate-temperature solid oxide fuel cells *Chin. Chem. Lett.* **33** 674–82
[41] Chen K, Ai N and Jiang S P 2012 Reasons for the high stability of nano-structured $(La,Sr)MnO_3$ infiltrated Y_2O_3–ZrO_2 composite oxygen electrodes of solid oxide electrolysis cells *Electrochem. Commun.* **19** 119–22
[42] Chen Y *et al* 2017 A highly efficient and robust nanofiber cathode for solid oxide fuel cells *Adv. Energy Mater.* **7** 1601890
[43] Zhao F, Peng R and Xia C 2008 LSC-based electrode with high durability for IT-SOFCs *Fuel Cells Bull.* **2008** 12–16
[44] Shao Z and Haile S M 2004 A high-performance cathode for the next generation of solid-oxide fuel cells *Nature* **431** 170–3
[45] Liu B, Zhang Y and Zhang L 2009 Oxygen reduction mechanism at $Ba_{0.5}Sr_{0.5}Co_{0.8}Fe_{0.2}O_{3-\delta}$ cathode for solid oxide fuel cell *Int. J. Hydrog. Energy* **34** 1008–14
[46] Flura A, Nicollet C, Vibhu V, Zeimetz B, Rougier A, Bassat J M and Grenier J C 2016 Application of the adler-lane-steele model to porous $La_2NiO_{4+\delta}$ SOFC cathode: influence of interfaces with gadolinia doped Ceria *J. Electrochem. Soc.* **163** F523
[47] Gao J, Li Q, Zhang Z, Lü Z and Wei B 2021 A cobalt-free bismuth ferrite-based cathode for intermediate temperature solid oxide fuel cells *Electrochem. Commun.* **125** 106978
[48] Chen Y *et al* 2018 A highly active, CO_2-tolerant electrode for the oxygen reduction reaction *Energy Environ. Sci.* **11** 2458–66
[49] Du Z, Li K, Zhao H, Dong X, Zhang Y and Świerczek K 2020 A $SmBaCo_2O_{5+\delta}$ double perovskite with epitaxially grown $Sm_{0.2}Ce_{0.8}O_{2-\delta}$ nanoparticles as a promising cathode for solid oxide fuel cells *J. Mater. Chem.* A **8** 14162–70
[50] Sahibzada M, Benson S J, Rudkin R A and Kilner J A 1998 Pd-promoted $La_{0.6}Sr_{0.4}Co_{0.2}Fe_{0.8}O_3$ cathodes *Solid State Ion.* **113–115** 285–90
[51] Esquirol A, Brandon N P, Kilner J A and Mogensen M 2004 Electrochemical characterization of $La_{0.6}Sr_{0.4}Co_{0.2}Fe_{0.8}O_3$ cathodes for intermediate-temperature SOFCs *J. Electrochem. Soc.* **151** A1847
[52] Leonide A, Apel Y and Ivers-Tiffee E 2009 SOFC modeling and parameter identification by means of impedance spectroscopy *ECS Trans.* **19** 81
[53] Mamak M, Métraux G S, Petrov S, Coombs N, Ozin G A and Green M A 2003 Lanthanum strontium manganite/yttria-stabilized zirconia nanocomposites derived from a surfactant assisted co-assembled mesoporous phase *J. Am. Chem. Soc.* **125** 5161–75
[54] Zamudio-García J, Caizán-Juanarena L, Porras-Vázquez J M, Losilla E R and Marrero-López D 2022 Boosting the performance of $La_{0.8}Sr_{0.2}MnO_{3-\delta}$ electrodes by the incorporation of nanocomposite active layers *Adv. Mater. Interfaces* **9** 2200702
[55] Escudero M J, Aguadero A, Alonso J A and Daza L 2007 A kinetic study of oxygen reduction reaction on La_2NiO_4 cathodes by means of impedance spectroscopy *J. Electroanal. Chem.* **611** 107–16
[56] Endler-Schuck C, Joos J, Niedrig C, Weber A and Ivers-Tiffée E 2015 The chemical oxygen surface exchange and bulk diffusion coefficient determined by impedance spectroscopy of porous $La_{0.58}Sr_{0.4}Co_{0.2}Fe_{0.8}O_{3-\delta}$ (LSCF) cathodes *Solid State Ion.* **269** 67–79
[57] Ringuedé A and Fouletier J 2001 Oxygen reaction on strontium-doped lanthanum cobaltite dense electrodes at intermediate temperatures *Solid State Ion.* **139** 167–77